



Synthesis and characterization of lanthanum nickelate nanoparticles with Ruddlesden-Popper crystal structure for cathode materials of solid oxide fuel cells

MohammadNavid Haddadnezhad¹, Alireza Babaei¹, Mohammad Jafar Molaei^{*2}, Abolghasem Ataie¹

¹School of Metallurgy and Materials Engineering, College of Engineering, University of Tehran, Tehran, Iran.

²Faculty of Chemical and Materials Engineering, Shahrood University of Technology, Shahrood, Iran.

Received: 26 October 2020; Accepted: 10 December 2020

* Corresponding author email: m.molaei@shahroodut.ac.ir

ABSTRACT

Lanthanum nickelate with the chemical formula of $\text{La}_2\text{NiO}_{4+\delta}$ has attracted research interests during recent years, due to its high oxygen ion diffusivity for application as cathode material in solid oxide fuel cells (SOFCs). In this research, lanthanum nickelate with Ruddlesden–Popper (RP) crystal structure was synthesized via the co-precipitation method. The effects of $\text{OH}^-/\text{NO}_3^-$ molar ratio, $\text{La}^{3+}/\text{Ni}^{2+}$ molar ratio, co-precipitation temperature, and calcination temperature on the phase composition, thermal behavior, morphology, and electrochemical properties of the synthesized samples were investigated. Analysis of the X-ray diffractometry (XRD) patterns revealed that the optimum $\text{OH}^-/\text{NO}_3^-$ and $\text{La}^{3+}/\text{Ni}^{2+}$ molar ratios in the co-precipitation stage are 1.25 and 1.7, respectively. The formation of RP lanthanum nickelate is promoted by calcination of the co-precipitated powder at 1000 °C, while the calcination at lower temperatures may lead to the formation of perovskite (P) lanthanum nickelate. Scanning electron microscopy (SEM) studies showed that the mean particle size decreases from 428 to 332 nm by increasing the $\text{OH}^-/\text{NO}_3^-$ molar ratio from 1 to 1.5 while it increases from 67 to 183 nm by increasing the calcination temperature from 900 to 1000 °C. Simultaneous differential thermal analysis (DTA/TG) showed that the single RP lanthanum nickelate phase starts to form at 920 °C and fully formed at 960 °C. The electrochemical impedance spectroscopy data indicated that the cell with the electrode sintered at 1050 °C has the lowest polarization resistance. The polarization resistance reached $1 \Omega \text{ cm}^2$ at the testing temperature of 800 °C, for the electrode sintered at 1050 °C. Impedance curves of the electrode were fitted and simulated with two semicircles at high and low frequencies. The activation energy of 1.14 eV was calculated for the electrode polarization resistance of the lanthanum nickelate electrode.

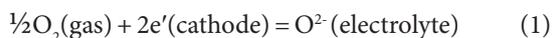
Keywords: Lanthanum nickelate; co-precipitation; SOFCs; Ruddlesden-popper.

1. Introduction

SOFCs are the cells that can convert the chemical energy of fuel into electricity by electrochemical oxidation which are promising cost-effective and highly efficient energy providers with minimal emission [1-4]. In SOFCs, there are

three main parts of a dense electrolyte, anode, and cathode which convert the chemical energy of a fuel and oxidant to electrical energy [5]. In SOFCs, the role of the cathode is generating oxygen ions from molecular oxygen which then oxygen ion migrates to the anode through

the electrolyte. The oxygen reduction reaction occurs in the cathode by the following reaction [6]:



The enhancement of durability and performance of the oxygen electrode in SOFCs and solid oxide electrolysis cells (SOECs) is a key factor in the performance of this electrode since it degrades in operating conditions. The oxides with alkaline earth metal elements like Ba or Sr lead to the formation of undesirable products. Therefore, finding oxides without alkaline earth metal elements has received great research interest in recent years [7].

The $\text{A}_2\text{BO}_{4+\delta}$ (A: a rare earth element; B: Cu, Fe, Ni) layered perovskite structures have found applications in SOFCs as the cathode materials [8, 9]. Rare earth nickelates, with an RP structure (K_2NiF_4 -type structure), can be used in oxygen electrodes in intermediated temperature solid oxide electrochemical devices [10]. Rare earth nickelates, with the formula of $\text{Ln}_2\text{NiO}_{4+\delta}$ (Ln=La, Sm, Pr, Nd, etc.) with alternating blocks of perovskite and rock-salt layers (LnNiO_3 and Ln_2O_2 , respectively) have shown to be as superior cathode materials for SOFCs. The obtained high oxygen surface exchange coefficients and oxygen ion diffusivities of these materials are due to their layered structure which can accommodate excess lattice oxygen in interstitial sites [11]. $\text{Ln}_2\text{NiO}_{4+\delta}$ materials, members of the RP series family, under high p_{O_2} atmospheres can accommodate excess interstitial oxygen and can withstand at low p_{O_2} atmospheres by loss of oxygen [7]. This type of $\text{Ln}_2\text{NiO}_{4+\delta}$ nickelates has satisfactory electrochemical, catalytic, and electronic conductivity [9, 12-15].

The electrochemical properties of $\text{Ln}_2\text{NiO}_{4+\delta}$ oxides have been extensively investigated in recent years [16-20]. It was reported that praseodymium-containing oxide has a higher electrochemical activity but suffers from decomposing in oxidizing atmospheres below 900 °C. The $\text{La}_2\text{NiO}_{4+\delta}$ is preferred to $\text{Pr}_2\text{NiO}_{4+\delta}$ since it is stable in oxidizing atmospheres below 900 °C [10]. Among the studied RP nickelates, $\text{La}_2\text{NiO}_{4+\delta}$ (LNO) has shown an enhanced value of the oxygen surface exchange coefficient (k) compared to the mixed conductors based on Sr-doped LaMnO_3 [8]. The oxygen excess in $\text{La}_2\text{NiO}_{4+\delta}$ is due to the interstitial oxygen into the rock salt layers and holes in the LaNiO_3 perovskite layers. The number of interstitial oxygen and holes are equivalent to keep the charge neutrality [21].

The excess oxygen in $\text{La}_2\text{NiO}_{4+\delta}$ is an important factor for the exhibited ionic conduction of the interstitial oxygen ion seen in this material [22]. Both computational and experimental results revealed that an interstitialcy diffusion mechanism is responsible for the diffusion along ab plane (almost three orders of magnitude higher than the diffusion along the c-axis) [9, 23]. The activation energy for this diffusion process is lower than other well-known ionic conductors such as yttria-stabilized-zirconia [23, 24]. Doping with different elements has been used to improve the electrochemical properties of $\text{La}_2\text{NiO}_{4+\delta}$ [25-29]. Due to the exceptional properties, La_2NiO_4 has been widely investigated during recent years [23, 30-35].

In the current research, the conditions for the synthesis of La_2NiO_4 through co-precipitation were systematically studied. The effects of synthesis parameters such as $\text{OH}^-/\text{NO}_3^-$ molar ratio, $\text{La}^{3+}/\text{Ni}^{2+}$ molar ratio, co-precipitation, and calcination temperatures on the powder particle characteristics were also investigated. Furthermore, the electrochemical properties of the produced La_2NiO_4 phase under the optimum synthesis conditions have been evaluated.

2. Experimental procedure

2.1. Materials

Analytical grades of nickel nitrate ($\text{Ni}(\text{NO}_3)_2 \cdot 6\text{H}_2\text{O}$, JHD), lanthanum oxide (La_2O_3 , Merck), nitric acid (HNO_3 , Mojalali), sodium hydroxide (NaOH, Merck), yttria-stabilized zirconia ($\text{Zr}_{0.92}\text{Y}_{0.08}\text{O}_{2-\delta}$, Tosoh), gadolinia doped ceria ($\text{Gd}_{0.1}\text{Ce}_{0.9}\text{O}_{1.95}$, Fuel cell materials Co.), and polyvinyl butyral ($(\text{C}_8\text{H}_{14}\text{O}_2)_n$, Kuraray) were used in this research.

2.2. Synthesis of lanthanum nickelate nanoparticles

Lanthanum nickelate nanoparticles were synthesized through the co-precipitation method. Briefly, for the $\text{La}^{3+}/\text{Ni}^{2+}$ molar ratio of two, 0.0078 mol of nickel nitrate was dissolved in 70 mL deionized water, and 0.0078 mol lanthanum oxide was dissolved in 5 mL of a solution of nitric acid and deionized water to obtain the required $\text{OH}^-/\text{NO}_3^-$ molar ratio for the mixed solutions. Subsequently, the solutions were mixed and heated to reach the desired temperature. Different temperatures of 25, 50, and 85 °C were investigated as the co-precipitation temperature. Then, sodium

hydroxide was added drop-wise to the mixed solution, while keeping the temperature steady for 1 h. The synthesis procedure was performed for different $\text{OH}^-/\text{NO}_3^-$ molar ratios of 1, 1.15, 1.25, and 1.5. The synthesis of the lanthanum nickelate was repeated with different $\text{La}^{3+}/\text{Ni}^{2+}$ molar ratios of 1.7, 1.8, and 2.2 by keeping the Ni^{2+} moles fixed and varying the La^{3+} moles in the solution. The studied co-precipitation temperatures for the samples were 27, 50, and 85 °C. The precipitates were filtered and washed several times and then were dried at 60 °C for 12 h. The dried precipitates were calcined at different temperatures in the range of 800-1100 °C for 2 h.

2.3. Fabrication of cathode cell

For the fabrication of yttria-stabilized zirconia (YSZ) electrolyte, 1.2 g of YSZ powder and 0.24 g polyvinyl butyral were mixed in ethanol, and the mixture was dried at 60 °C. The resultant agglomerates were then ground to fine powder in a mortar. The powder was pressed under 100 MPa pressure, followed by sintering at 1500 °C for 4 h. The surface of the produced pellets was polished using sandpaper. A thin interlayer of gadolinia doped ceria (GDC) was screen-printed on both sides of pellets followed by sintering at 1250 °C for 2 h, to achieve an almost 4 μm thick interlayer. Lanthanum nickelate powder (synthesized with $\text{OH}^-/\text{NO}_3^- = 1.25$, $\text{pH} = 13$, $\text{La}^{3+}/\text{Ni}^{2+} = 1.7$, co-precipitation temperature = 85 °C, and calcination temperature = 1000 °C) was mixed with ink vehicle (Full cell materials Co.) in a mortar, and a circle-shaped electrode layer with a surface area of 0.32 cm^2 was hand-painted on the top of GDC interlayer on both sides. The painted pellets were dried in an oven and subsequently heat-treated for 2 h at different temperatures of 950, 1050, 1100, and 1150 °C. Symmetric cell configuration was selected for the electrochemical measurements. Pt mesh was used as the current collector.

2.4. Characterization techniques

Phase analysis was performed with a Philips PW-1730 diffractometer operating at 40 kV, 30 mA with CuK_α radiation. The measurements were recorded in $2\theta = 20-80^\circ$ with a step size of 0.02° . The morphology of the synthesized nanoparticles was studied with a scanning electron microscope (SEM, ZEISS Sigma VP, Jena, Germany). The mean particle size was determined by averaging 100 particles of each sample using Image J software. Simultaneous

thermal analysis (STA) was done on a BAHR STA 503. A potentiostat/galvanostat (PARSTAT 2273) was applied for the electrochemical impedance spectroscopy (EIS) in the frequency range of 0.1 Hz to 100 kHz in the temperature range of 600-800 °C. The measurements were conducted under open circuit conditions with an AC signal amplitude of 10 mV. Fitting and simulation of EIS data was performed using ZSimpWin software.

3. Results and discussion

3.1. Effect of $\text{OH}^-/\text{NO}_3^-$ molar ratio

Figure 1 shows the XRD patterns of the synthesized samples with different $\text{OH}^-/\text{NO}_3^-$ molar ratios after calcination at 1000 °C. It can be seen that the sample processed with an $\text{OH}^-/\text{NO}_3^-$ molar ratio of 1 contains RP lanthanum nickelate and lanthanum nickelate perovskite as major phases together with the small amount of lanthanum oxide phase. By increasing the $\text{OH}^-/\text{NO}_3^-$ molar ratio, the lanthanum oxide phase volume fraction decreases and reaches its minimum value in a ratio of 1.25.

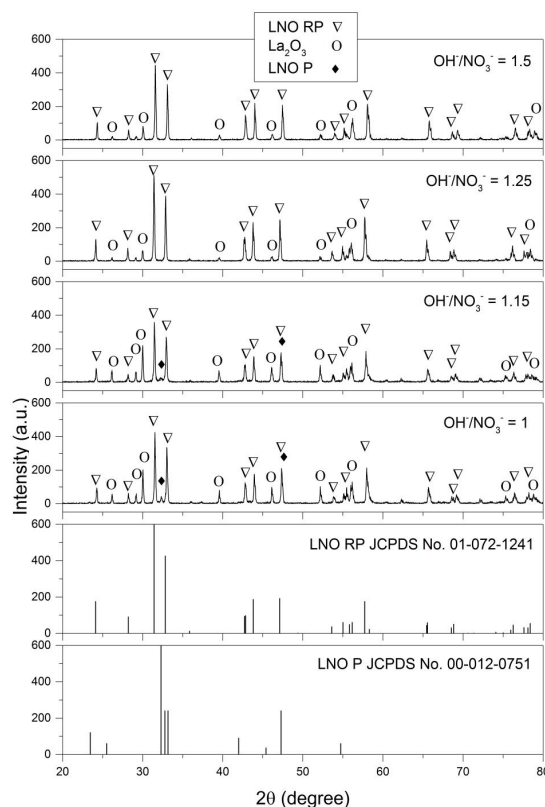


Fig. 1- XRD patterns of synthesized samples with different $\text{OH}^-/\text{NO}_3^-$ molar ratios. The synthesis conditions are as follow: $\text{La}^{3+}/\text{Ni}^{2+} = 2$, co-precipitation temperature = 50 °C, and calcination temperature = 1000 °C. (LNO RP and LNO P are RP and perovskite $\text{La}_2\text{NiO}_{4+\delta}$, respectively).

Therefore, the optimum $\text{OH}^-/\text{NO}_3^-$ molar ratio for the formation of RP lanthanum nickelate was found to be 1.25. The observed LaNiO_3 perovskite phase can be formed as a result of the reaction (2).



Figure 2a shows the SEM images of the synthesized samples with different $\text{OH}^-/\text{NO}_3^-$ ratios. The particle size distribution is also exhibited in Figure 2b. The measurements reveal that the morphology of the particles is almost similar for

the different $\text{OH}^-/\text{NO}_3^-$ molar ratios, while the mean particle size decreases from 428 nm to 332 nm by increasing the $\text{OH}^-/\text{NO}_3^-$ molar ratio from 1 to 1.5. The reduction of the mean particle size might be due to an enhanced driving force for the nucleation at a higher $\text{OH}^-/\text{NO}_3^-$ molar ratio. The higher number of the nuclei and their subsequent growth results in smaller particle size at a higher $\text{OH}^-/\text{NO}_3^-$ molar ratio, compared to the sample synthesized under lower $\text{OH}^-/\text{NO}_3^-$ molar ratio conditions with a decreased driving force for the nucleation.

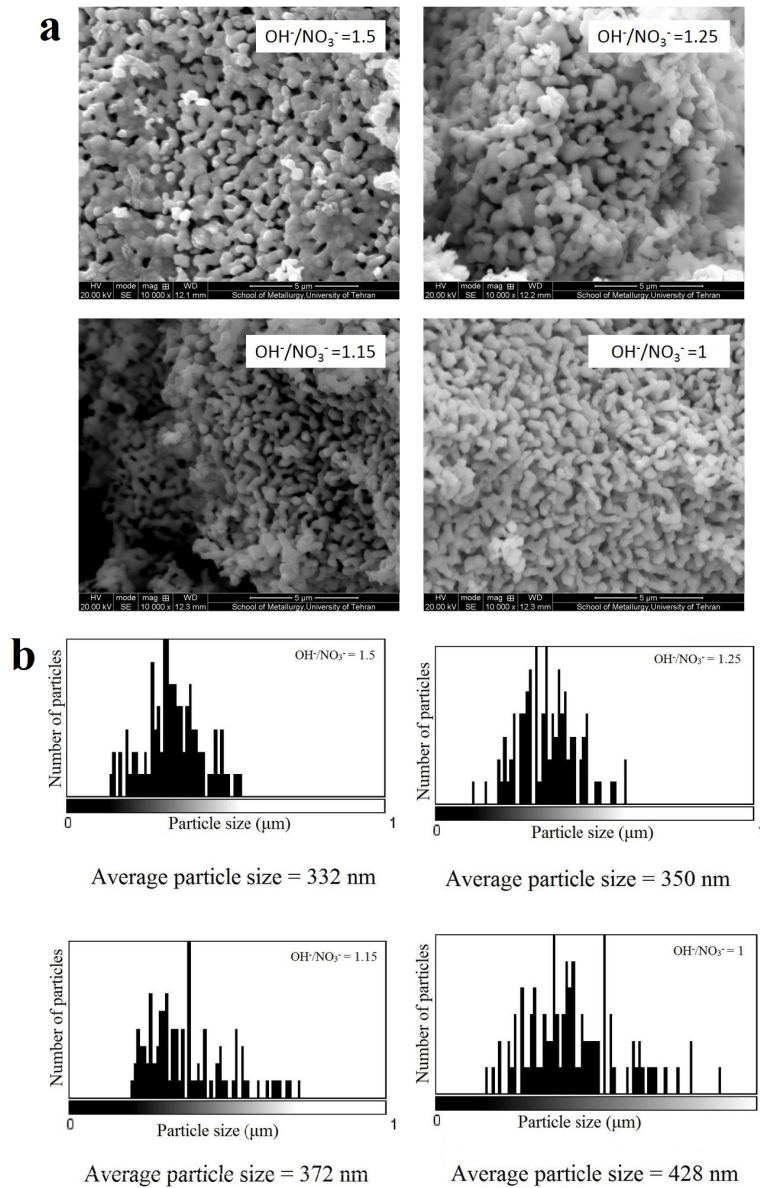


Fig. 2- The synthesized samples with different $\text{OH}^-/\text{NO}_3^-$ molar ratios: (a) The SEM images, (b) Particle size distribution and mean particle size. The synthesis conditions are as follow: $\text{La}^{3+}/\text{Ni}^{2+}=2$, co-precipitation temperature=50 °C, and calcination temperature=1000 °C).

3.2. Effect of the co-precipitation temperature

Figure 3 shows the XRD patterns of the synthesized samples at different co-precipitation temperatures after calcination at 1000 °C. The sample with a co-precipitation temperature of 27 °C consists of RP lanthanum nickelate and La_2O_3 after calcination. By increasing the co-precipitation temperature to 50 °C the peaks of RP lanthanum nickelate become more intensive. However, the co-precipitation temperature of 85 °C leads to the formation of perovskite lanthanum nickelate together with former phases of RP lanthanum nickelate and La_2O_3 after calcination. It was observed that by increasing the co-precipitation temperature from 27 to 85 °C, the pH of the solution decreases from 13 to 10, respectively. It has been reported that increasing the pH value from 10 to 13 leads to an increase in the precipitation of the lanthanum hydroxide [36]. Therefore, in the synthesis conditions of pH of 13 and the co-precipitation temperature of 27 °C, the precipitation of lanthanum oxide is preferred. Although the sample synthesized at 50 °C exhibits higher purity for the RP lanthanum nickelate phase after calcination, the sample treated at 85 °C was chosen as the sample for further investigation due to its smaller mean particle size.

The effect of co-precipitation temperature on particle morphology and mean particle size are illustrated in Figure 4. As was mentioned earlier, by increasing the synthesis temperature, the pH of the solution decreases which may affect the particle size. It is observed that the sample synthesized at a

higher co-precipitation temperature has a smaller mean particle size. The reduction in the particle size with a decrease in pH in the co-precipitation synthesis method has been reported before. The particle growth kinetics is favored at higher pH values during the co-precipitation synthesis [37]. The particle size distribution for the samples co-precipitated at room temperature and 85 °C is almost identical.

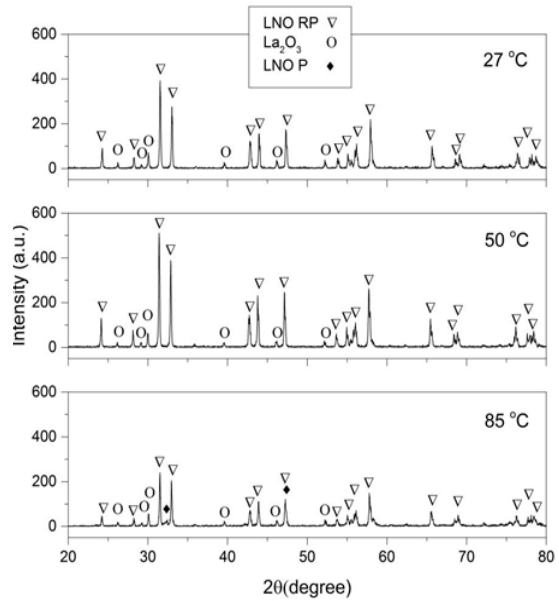


Fig. 3- XRD patterns of synthesized samples at different co-precipitation temperatures. The synthesis conditions are as follow: $\text{OH}^-/\text{NO}_3^- = 1.25$, $\text{La}^{3+}/\text{Ni}^{2+} = 2$, calcination temperature = 1000 °C. (LNO RP and LNO P are RP and perovskite $\text{La}_2\text{NiO}_{4+\delta}$, respectively).

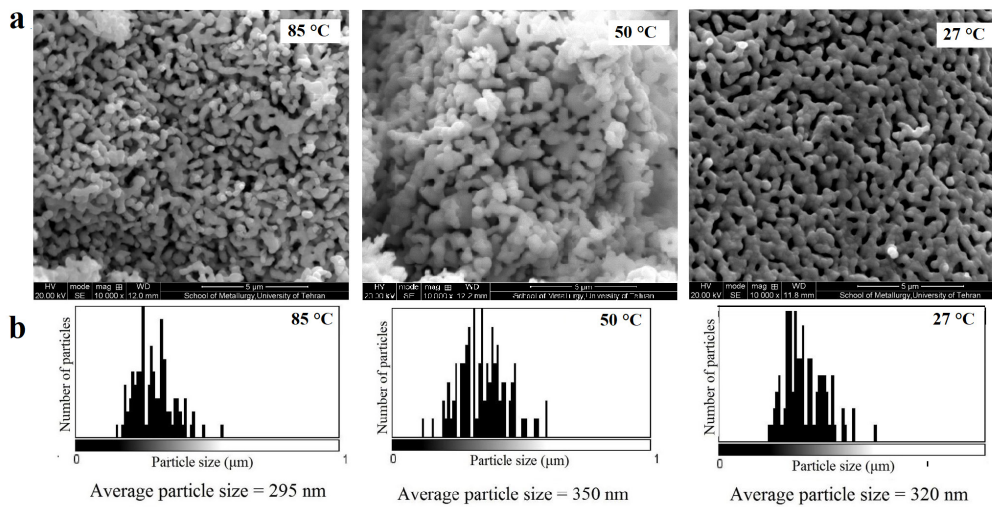


Fig. 4- The synthesized samples with different co-precipitation temperatures: (a) The SEM images, (b) Particle size distribution and mean particle size data. The synthesis conditions are as follow: $\text{OH}^-/\text{NO}_3^- = 1.25$, $\text{La}^{3+}/\text{Ni}^{2+} = 2$, calcination temperature = 1000 °C.

3.3. Effect of La³⁺/Ni²⁺ molar ratio

XRD patterns of the samples synthesized with different La³⁺/Ni²⁺ molar ratios are illustrated in Figure 5. The sample with a La³⁺/Ni²⁺ molar ratio of 2.2 consists of RP lanthanum nickelate, perovskite phase, and lanthanum oxide. By decreasing the La³⁺/Ni²⁺ molar ratio from 2.2 to 1.7, the amount of the formed lanthanum oxide decrease. The higher amounts of the formed lanthanum oxide in the samples with a higher La³⁺/Ni²⁺ molar ratio is due to the lower amounts of available Ni²⁺ ions for the formation of lanthanum nickelate phase. The remained La³⁺ cannot impart in the structure of lanthanum nickelate and consequently, will be oxidized. It can be concluded that in the stoichiometric molar ratio of La³⁺/Ni²⁺, lanthanum oxide will exist in the final product whereas, by a decrease in this ratio, the amount of this phase decreases. Furthermore, the perovskite phase was formed in the samples with La³⁺/Ni²⁺ molar ratios of 2.2, 2, and 1.7. It has been reported that the perovskite phase forms in the La³⁺/Ni²⁺ molar ratios smaller than 1.8 [38]. The optimum La³⁺/Ni²⁺ molar ratio of 1.7 was chosen for the synthesis of pure RP lanthanum nickelate due to the absence of detectable lanthanum oxide in its XRD pattern. The SEM images of the samples synthesized with different La³⁺/Ni²⁺ molar ratios are presented in Figure 6. The samples with higher La³⁺/Ni²⁺ molar ratios show a larger mean particle size.

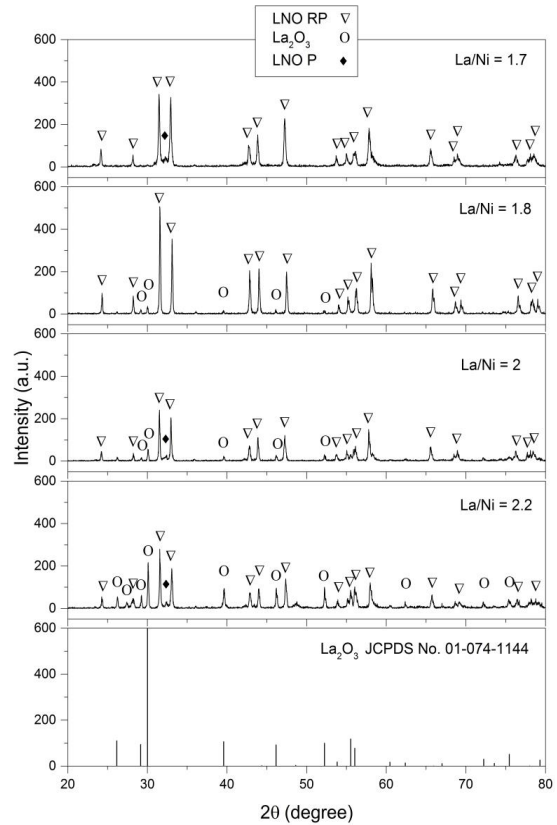


Fig. 5- XRD patterns of synthesized samples with different La³⁺/Ni²⁺ molar ratios. The synthesis conditions are as follow: OH⁻/NO₃⁻=1.25, pH of 10, co-precipitation temperature=85 °C, calcination temperature=1000 °C. (LNO RP and LNO P are RP and perovskite La₂NiO_{4+δ}, respectively).

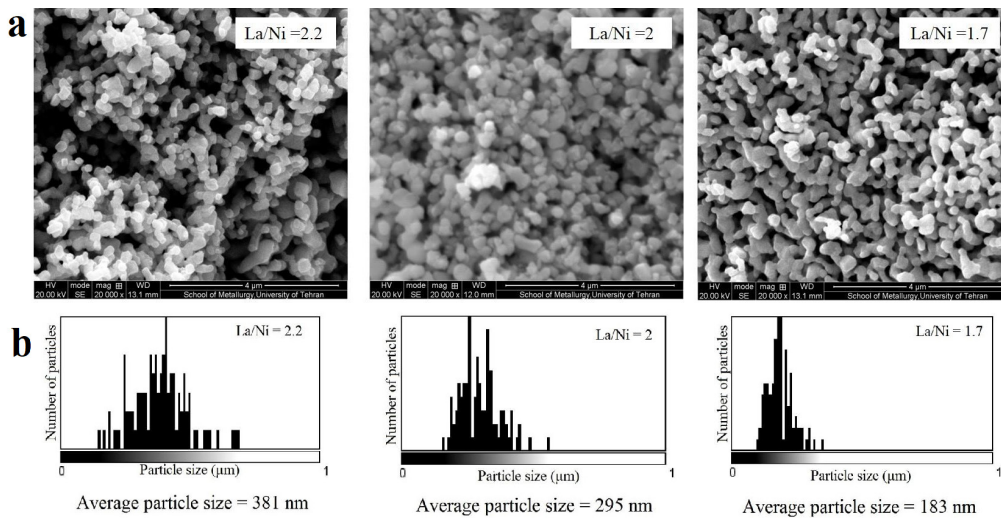


Fig. 6- The synthesized samples with different La³⁺/Ni²⁺ molar ratios, (a) The SEM images, (b) Particle size distribution and mean particle size data. The synthesis conditions are as follow: OH⁻/NO₃⁻=1.25, pH of 10, co-precipitation temperature=85 °C, calcination temperature=1000 °C.

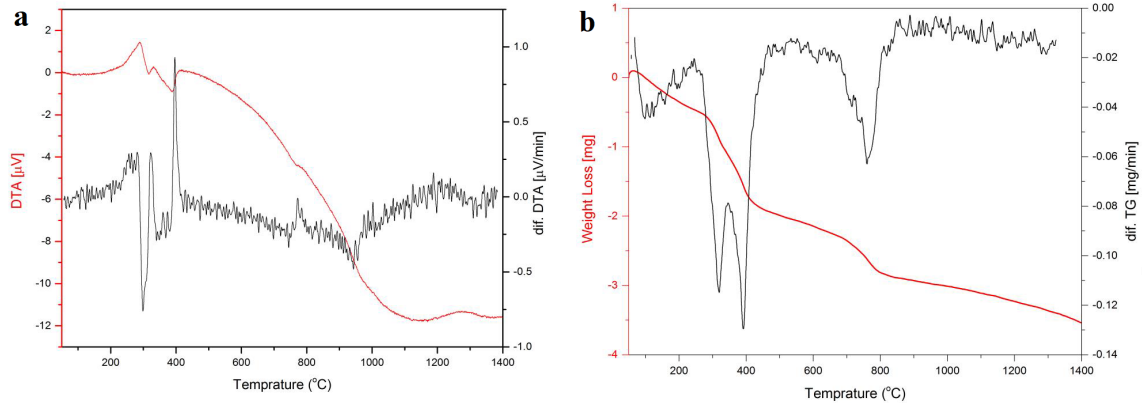


Fig. 7- The (a) DTA/DDTA and (b) TG/DTG traces of the sample synthesized with $\text{OH}^-/\text{NO}_3^- = 1.25$, $\text{La}^{3+}/\text{Ni}^{2+} = 1.7$, and co-precipitation temperature = 85°C .

3.4. Effect of calcination temperature

Thermal analysis was performed to evaluate the stability range of the RP lanthanum nickelate phase. The DTA/DDTA and TG/DTG results of the sample synthesized with $\text{OH}^-/\text{NO}_3^- = 1.25$, $\text{La}^{3+}/\text{Ni}^{2+} = 1.7$, and co-precipitation temperature = 85°C are shown in Figure 7 and the corresponding XRD patterns of this sample after calcination at different temperatures are illustrated in Figure 8. The peaks in the differential of the DTA diagram below 130°C corresponds to the removal of adsorbed water which is accompanied by a 3% weight reduction as is evidenced by the DTG diagram. The large peaks from 280 to 390°C in the DTA curve are responsible for 27% weight reduction. The peaks before 600°C are related to the burnout of pyrolyzed organics and decomposition of organics and nitrate species [39]. The exothermic peak at 760°C is attributed to the transformation of lanthanum oxide into the perovskite lanthanum nickelate (Figure 7). The endothermic peak starting at 920°C which is ended at 960°C is accompanied by a 1% weight reduction and corresponds to the formation of RP lanthanum nickelate as can be concluded from the XRD patterns in Figure 8. The formation of RP lanthanum nickelate occurs by the reaction between LaNiO_3 and La_2O_3 as it was depicted in reaction (1) [40]. The formation of $\text{La}_2\text{NiO}_{4+\delta}$ from the solutions of metal nitrates has been reported to occur above 700°C [39]. The lanthanum oxide and perovskite lanthanum nickel oxide converts into the RP lanthanum nickelate [40]. The exothermic peak at 1000°C might belong to the converting of the RP lanthanum nickelate to the lanthanum nickel oxide with other stoichiometry.

The XRD patterns of the calcined samples in

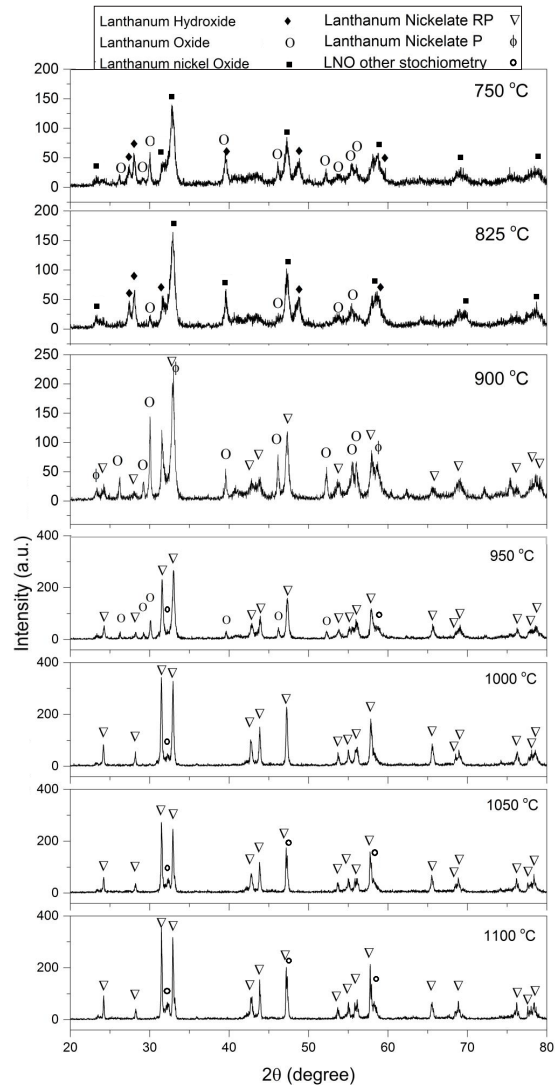


Fig. 8- XRD patterns of the sample synthesized with $\text{OH}^-/\text{NO}_3^- = 1.25$, $\text{La}^{3+}/\text{Ni}^{2+} = 1.7$, and co-precipitation temperature = 85°C after calcination at different temperatures.

Figure 8 show more progress in the formation of the RP lanthanum nickelate phase at 1000 °C while at lower calcination temperature perovskite phase exists in the calcined samples. Since the atomic ratio of $\text{La}^{3+}/\text{Ni}^{2+}$ in the perovskite phase is 1, therefore, more Ni^{2+} is consumed which leads to the formation of lanthanum oxide. Increasing the calcination temperature above 1000 °C leads to the formation of lanthanum nickelate with different stoichiometries (e.g. $\text{La}_3\text{Ni}_2\text{O}_7$ and $\text{La}_4\text{Ni}_3\text{O}_{10}$).

The calcination temperature should be high enough to promote the formation of RP lanthanum nickelate. The mean particle size increase from 67 to 183 nm by increasing the calcination temperature from 900 °C to 1000 °C (Figure 9). The particle size distribution becomes less uniform by increasing the calcination temperature. Partial sintering of the particles could be observed in the SEM image of the sample calcined at 1000 °C

3.5. Electrochemical studies

The RP lanthanum nickelate powder with optimum synthesis conditions ($\text{OH}/\text{NO}_3=1.25$, $\text{La}^{3+}/\text{Ni}^{2+}=1.7$, co-precipitation temperature=85 °C, and calcination temperature=1000 °C) was used for the fabrication of electrochemical cells. Figure 10 shows the results of electrochemical impedance measurement of the fabricated cells with different sintering temperatures, taken at the testing temperature of 800 °C. For the sake of improved comparability, the ohmic resistance of the EIS curves is set to zero in Figure 10a. It is observed

that by increasing the sintering temperature, the ohmic resistance of the cell decreases (Figure 10b). In all samples, a major part of the ohmic resistance is due to the YSZ electrolyte. The cross-sectional observation of the YSZ electrolyte shows that it consists of a high-density structure that minimizes the effect of porosities on ohmic resistance (Figure S2). The decrease in the ohmic resistance by increasing the sintering temperature is due to the better adhesion of the LNO electrode layer to GDC interlayer as well as improving particle connection within the active LNO layer which facilitates the charge transport characteristic and this will in turn might reduce the polarization resistance via a reduction in the current constriction effect.

By increasing the sintering temperature, the electrode polarization resistance decreases first and then increases, with its minimum at 1050 °C. Increasing the sintering temperature from 1050 °C to 1150 °C increases the contribution of polarization resistances associated with both high and low-frequency processes. The increase in the polarization resistance associated with the high frequency portion of the EIS curve (~10kHz) might be caused by the formation of electrically insulator oxide phases within the LNO-GDC interface, which impedes the ionic charge transfer between LNO and GDC layers [41]. Figure S1 shows that by the heat treatment of LNO and GDC at 1050 °C and 1150 °C, the XRD peaks of the starting materials vanish, and those of other undesired phases appear. Furthermore, an increase in the

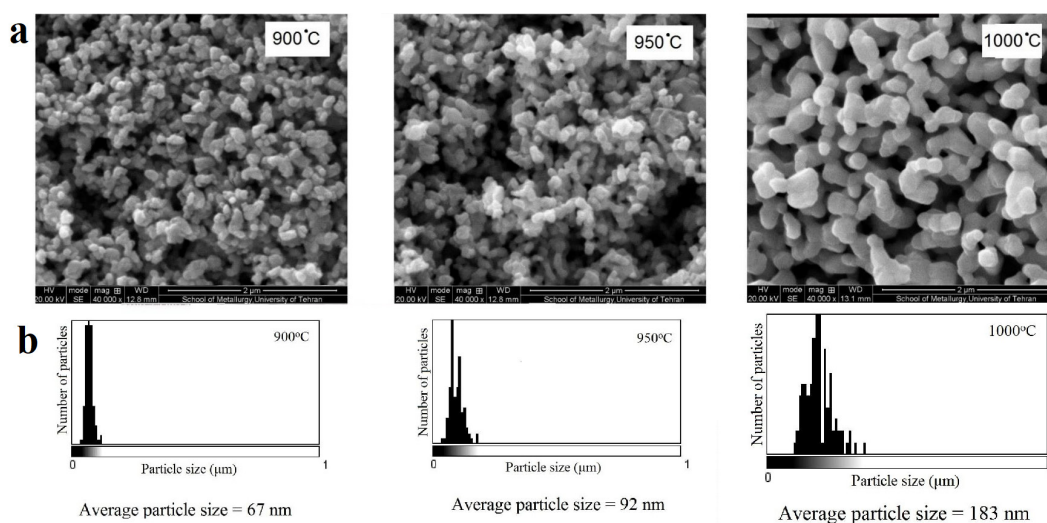


Fig. 9- The synthesized samples calcined at different temperatures, (a) The SEM images, (b) Particle size distribution and mean particle size data. The synthesis conditions are as follow: $\text{OH}/\text{NO}_3=1.25$, pH of 13, $\text{La}^{3+}/\text{Ni}^{2+}=1.7$, co-precipitation temperature=85 °C.

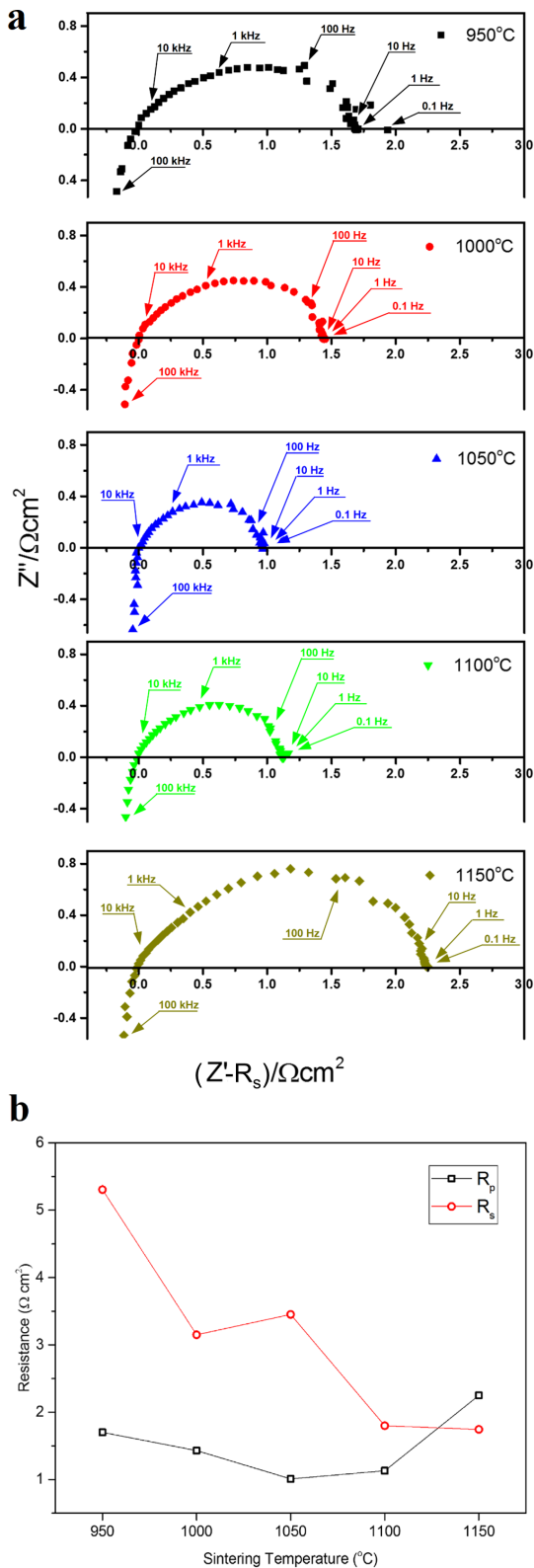


Fig. 10- (a) Electrochemical impedance curves, and (b) Ohmic and electrode polarization resistance of the cells fabricated at 950-1150°C at the testing temperature of 800 °C.

electrode polarization resistance associated with the low frequencies is observable in the EIS curves of Figure 10a (~10-100Hz), which is due to the particle coarsening and subsequent decrease in the available free surface for catalytic oxygen reduction reaction. The reduction of polarization resistance with increasing the sintering temperature from 950 °C to 1050 °C might be due to an improvement in sintering and attachment of the particles which facilitates the oxygen ions and electric charges transfer. Generally, the polarization resistance of the oxygen electrodes in solid oxide cells is influenced by several factors including oxygen surface exchange, ion transfer at the cathode-electrolyte interface, oxygen adsorption/dissociation, oxygen atomic diffusion, gas-phase diffusion, and charge transfer reactions [42].

Figure 11 shows the SEM images of the cross-sections of the cells that their electrode was fabricated at temperatures in the range of 950-1150 °C. As can be seen in Figure 11, by increasing the sintering temperature, the particle size of the lanthanum nickelate increases. Increasing the particle size, decreases the surface to volume ratio, and hurts the catalytic activity of lanthanum nickelate. Increasing the particle size with increasing the sintering temperature reduces the active surfaces which consequently increases the polarization resistance in the low frequency range [42]. High porosity with interconnected paths is preferred for the enhanced oxygen diffusion and cell performance [43]. Therefore, there should be an optimum particle size for the best performance of the cell which occurs at temperatures between 950 to 1150 °C in the fabricated cathodes. The SEM images also show that the GDC layer is not dense enough (which is also supported by the observation of very large R_s values). This, in turn, will create a prominent bottleneck on the oxygen journey towards the electrolyte, and hence major impedance contributions were observed in the high-frequency range. The cross-sections of the fabricated cells also show that the proper sintering has only occurred at higher temperatures, while in the cathodes fabricated at lower temperatures, lack of appropriate connection between the lanthanum nickelate and GDC interlayer, prevents electron and ions transportation. The sintering temperature should be high enough to ensure particle surface adhesion, and low enough to prevent the formation of undesired phases at the interfaces of the particles. Therefore, according to the polarization resistance

and the morphology of the particles and cell cross-section, the cells fabricated at 1050 °C has the optimum conditions. Further chemical analysis of the cell cross-section is represented in Figure S3.

The Nyquist plots of the cells with cathodes fabricated at 1050 °C at different testing

temperatures of 600 to 800 °C are illustrated in Figure 12a. Each Nyquist curve consists of two semi-circles according to the data obtained by curve fitting. The equivalent circuit used for the curve fitting is shown in Figure 12b. By increasing the testing temperature, the summit frequencies of

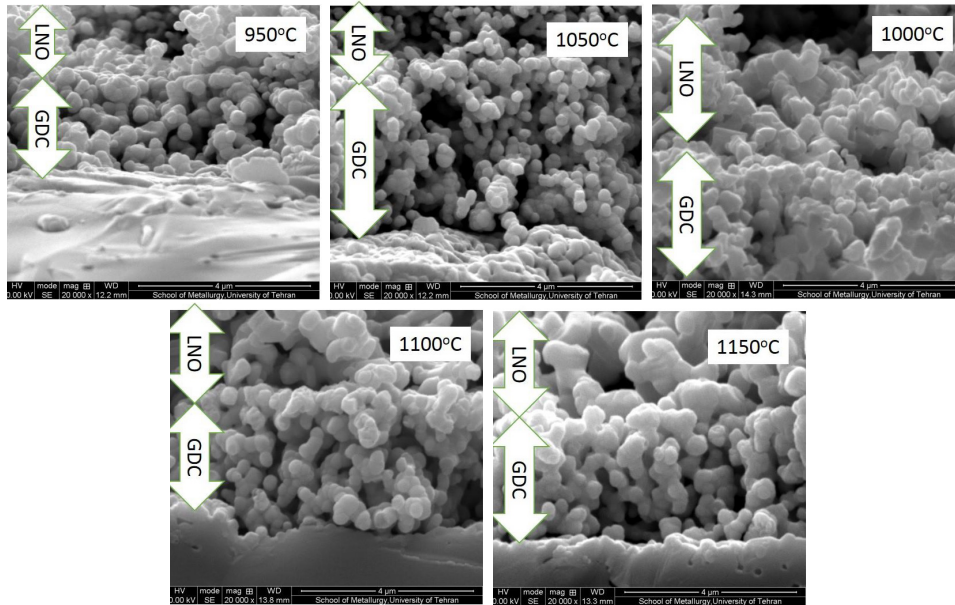


Fig. 11- SEM images of the cell cross-sections sintered at different temperatures in the range of 950 -1150 °C.

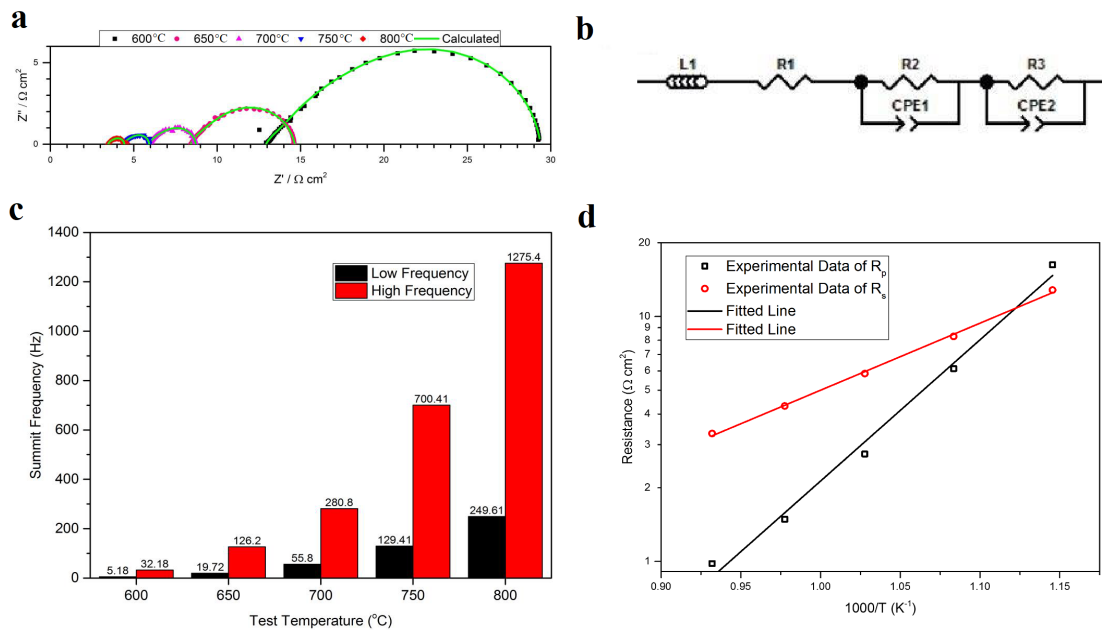


Fig. 12- (a) Nyquist curves of the cells with cathodes sintered at 1050 °C at different testing temperatures of 600-800 °C. (b) The equivalent circuit for electrochemical impedance data-fitting, (c) The summit frequency of the Nyquist curves at high-frequency and low-frequency semi-circles with electrodes fabricated at 1050 °C. D) Arrhenius plots for the ohmic and polarization resistance of cathod fabricated at 1050 °C.

the curves shift to higher frequencies and this effect is more intense for the high-frequency semi-circle (Figure 12c). By increasing the testing temperature, the high-frequency intercept of the Nyquist curves shift to the left and the semi-circles become smaller which is an indication of the decrease in both ohmic and polarization resistances. The resistance decrease is more pronounced for the high-frequency curves, compared to low-frequency ones. This phenomenon shows that through increasing the temperature, oxygen ion charge transportation between electrode and electrolyte which is a high-frequency reaction has a stronger effect on the reduction of polarization resistance, compared to the oxygen surface exchange and oxygen reduction which are attributed to the low-frequency range. Figure 12d shows the Arrhenius plot for the ohmic and electrode polarization resistance of the cell, fabricated at 1050 °C. Activation energy for the ohmic resistance (after deduction of resistance of connecting wires) is calculated around 0.54, which is less than those reported in the literature. The reason for this discrepancy might be the presence of porous GDC interlayer that significantly affects the migration of oxygen ions. Activation energy for the electrode polarization resistance is calculated equal to 1.14 eV, which is well comparable with the reported data in the literature [43].

4. Conclusions

The synthesis of RP phase lanthanum nickelate ($\text{La}_2\text{NiO}_{4+\delta}$) through the co-precipitation method and subsequent calcination was studied. The effects of synthesis parameters such as $\text{OH}^-/\text{NO}_3^-$ molar ratio, $\text{La}^{3+}/\text{Ni}^{2+}$ molar ratio, co-precipitation temperature, and calcination temperature on the phase constitution and particle morphology were investigated. The optimum $\text{OH}^-/\text{NO}_3^-$ ratio for the formation of RP lanthanum nickelate was found to be 1.25. The stoichiometric ratio of $\text{La}^{3+}/\text{Ni}^{2+}$ causes the existence of lanthanum oxide in the final product. The $\text{La}^{3+}/\text{Ni}^{2+}$ molar ratio of 1.7 can be considered as the optimum molar ratio for the production of RP lanthanum nickelate. The RP $\text{La}_2\text{NiO}_{4+\delta}$ can be synthesized by calcination at 1000 °C while the samples calcined at lower temperatures may contain the perovskite phase in the final product. The mean particle size increase from 67 to 183 nm by increasing the calcination temperature from 900 °C to 1000 °C. Among the cells with different sintering temperatures, the cell with the electrode sintered at 1050 °C had the lowest

resistance. It was concluded that by increasing the temperature, oxygen ion charge transfer between the electrode and electrolyte has a pronounced effect on the reduction of polarization resistance, compared to the oxygen surface exchange, and oxygen reduction reactions. The results showed that by controlling the synthesis parameters, the RP $\text{La}_2\text{NiO}_{4+\delta}$ phase with desirable particle size and electrochemical properties can be synthesized for application as cathode material for SOFCs.

References

1. Bu Y, Joo S, Zhang Y, Wang Y, Meng D, Ge X, et al. A highly efficient composite cathode for proton-conducting solid oxide fuel cells. *Journal of Power Sources*. 2020;451:227812.
2. Basbus J, Arce M, Troiani H, Su Q, Wang H, Caneiro A, et al. Study of $\text{BaCe}_{0.4}\text{Zr}_{0.4}\text{Y}_{0.2}\text{O}_{3-\delta}/\text{BaCe}_{0.8}\text{Pr}_{0.2}\text{O}_{3-\delta}$ (BCZY/BCP) bilayer membrane for Protonic Conductor Solid Oxide Fuel Cells (PC-SOFC). *International Journal of Hydrogen Energy*. 2020;45(8):5481-90.
3. Pei K, Zhou Y, Xu K, He Z, Chen Y, Zhang W, et al. Enhanced Cr-tolerance of an SOFC cathode by an efficient electro-catalyst coating. *Nano Energy*. 2020;72:104704.
4. Baba S, Ohguri N, Suzuki Y, Murakami K. Evaluation of a variable flow ejector for anode gas circulation in a 50-kW class SOFC. *International Journal of Hydrogen Energy*. 2020;45(19):11297-308.
5. Abdalla AM, Hossain S, Azad AT, Petra PMI, Begum F, Eriksson SG, et al. Nanomaterials for solid oxide fuel cells: A review. *Renewable and Sustainable Energy Reviews*. 2018;82:353-68.
6. He T, Zhou Q, Jin F. Cathodes for Solid Oxide Fuel Cell. *Solid Oxide Fuel Cells*; Wiley; 2020. p. 79-112.
7. Laguna-Bercero MA, Monzón H, Larrea A, Orera VM. Improved stability of reversible solid oxide cells with a nickelate-based oxygen electrode. *Journal of Materials Chemistry A*. 2016;4(4):1446-53.
8. Kolchugin AA, Pikalova EY, Bogdanovich NM, Bronin DI, Pikalov SM, Plaksin SV, et al. Structural, electrical and electrochemical properties of calcium-doped lanthanum nickelate. *Solid State Ionics*. 2016;288:48-53.
9. Burriel M, Téllez H, Chater RJ, Castaing R, Veber P, Zaghrioui M, et al. Influence of Crystal Orientation and Annealing on the Oxygen Diffusion and Surface Exchange of $\text{La}_2\text{NiO}_{4+\delta}$. *The Journal of Physical Chemistry C*. 2016;120(32):17927-38.
10. Antonova EP, Khodimchuk AV, Tropin ES, Porotnikova NM, Farlenkov AS, Vlasov MI, et al. Influence of modifying additives on electrochemical performance of $\text{La}_2\text{NiO}_{4+\delta}$ -based oxygen electrodes. *Solid State Ionics*. 2020;346:115215.
11. Gong Y, Wang R, Banner J, Basu SN, Pal UB, Gopalan S. Improved Tolerance of Lanthanum Nickelate ($\text{La}_2\text{NiO}_{4+\delta}$) Cathodes to Chromium Poisoning Under Current Load in Solid Oxide Fuel Cells. *JOM*. 2019;71(11):3848-58.
12. Khamidy NI, Laurencin J, Ferreira Sanchez D, Monaco F, Charlot F, Djurado E. Durability of nanostructured $\text{LaPrNiO}_{4+\delta}$ electrode for solid oxide cells: Electrochemical, microstructural, and structural investigation. *Journal of Power Sources*. 2020;450:227724.
13. Morales-Zapata MA, Larrea A, Laguna-Bercero MA. Reversible operation performance of microtubular solid oxide cells with a nickelate-based oxygen electrode. *International Journal of Hydrogen Energy*. 2020;45(8):5535-42.

14. Vibhu V, Vinke IC, Eichel R-A, Bassat J-M, de Haart LGJ. Cobalt Substituted Lanthanide Nickelates ($\text{Ln}_2\text{Ni}_{1-x}\text{Co}_x\text{O}_{4+\delta}$, Ln = La, Pr; x=0, 0.1, 0.2) as High Performance Oxygen Electrodes for Solid Oxide Cells. *ECS Transactions*. 2019;91(1):1327-39.
15. Sakai M, Wang C, Okiba T, Soga H, Hashimoto T. Evaluation of stability of $\text{Pr}_2\text{-xNd}_x\text{NiO}_{4+\delta}$ by thermogravimetry under various oxygen partial pressures. *Journal of Thermal Analysis and Calorimetry*. 2019;142(1):139-47.
16. Sadykov VA, Pikalova EY, Kolchugin AA, Fetisov AV, Sadovskaya EM, Filonova EA, et al. Transport properties of Ca-doped Ln_2NiO_4 for intermediate temperature solid oxide fuel cells cathodes and catalytic membranes for hydrogen production. *International Journal of Hydrogen Energy*. 2020;45(25):13625-42.
17. Zhao K, Xu Q, Huang D-P, Chen M, Kim B-H. Microstructure and electrochemical properties of porous $\text{La}_2\text{NiO}_{4+\delta}$ electrodes spin-coated on $\text{Ce}_{0.8}\text{Sm}_{0.2}\text{O}_{1.9}$ electrolyte. *Ionics*. 2011;18(1-2):75-83.
18. Kim D, Lee KT. Effect of lanthanide (Ln=La, Nd, and Pr) doping on electrochemical performance of $\text{Ln}_2\text{NiO}_{4+\delta}$ -YSZ composite cathodes for solid oxide fuel cells. *Ceramics International*. 2021;47(2):2493-8.
19. Benamira M, Ringuedé A, Cassir M, Horwat D, Lenormand P, Ansart F, et al. Enhancing oxygen reduction reaction of YSZ/ $\text{La}_2\text{NiO}_{4+\delta}$ using an ultrathin $\text{La}_2\text{NiO}_{4+\delta}$ interfacial layer. *Journal of Alloys and Compounds*. 2018;746:413-20.
20. Wu X, Gu C, Cao J, Miao L, Fu C, Liu W. Investigations on electrochemical performance of $\text{La}_2\text{NiO}_{4+\delta}$ cathode material doped at A site for solid oxide fuel cells. *Materials Research Express*. 2020;7(6):065507.
21. Yoo Y-S, Choi M, Hwang J-H, Im H-N, Singh B, Song S-J. $\text{La}_2\text{NiO}_{4+\delta}$ as oxygen electrode in reversible solid oxide cells. *Ceramics International*. 2015;41(5):6448-54.
22. Chronos A, Parfitt D, Kilner JA, Grimes RW. Anisotropic oxygen diffusion in tetragonal $\text{La}_2\text{NiO}_{4+\delta}$: molecular dynamics calculations. *J Mater Chem*. 2010;20(2):266-70.
23. Maas K, Villepreux E, Cooper D, Salas-Colera E, Rubio-Zuazo J, Castro GR, et al. Tuning Memristivity by Varying the Oxygen Content in a Mixed Ionic-Electronic Conductor. *Advanced Functional Materials*. 2020;30(17):1909942.
24. Baeumer C, Schmitz C, Ramadan AHH, Du H, Skaja K, Feyrer V, et al. Spectromicroscopic insights for rational design of redox-based memristive devices. *Nature communications*. 2015;6:8610-.
25. Sadykov, V.A., Pikalova, E.Y., Kolchugin, A.A., Fetisov, A.V., Sadovskaya, E.M., Filonova, E.A., Ereemeev, N.F., Goncharov, V.B., Krasnov, A.V., Skriabin, P.I. and Shmakov, A.N., Transport properties of Ca-doped Ln_2NiO_4 for intermediate temperature solid oxide fuel cells cathodes and catalytic membranes for hydrogen production. *International Journal of Hydrogen Energy*, 2018.
26. Gilev AR, Kiselev EA, Cherepanov VA. Bulk Oxygen Diffusion and Surface Exchange Limitations in $\text{La}_2\text{-xSr}_x\text{Ni}_{1-y}\text{Fe}_y\text{O}_{4+\delta}$. *KnE Materials Science*. 2018;4(2):24.
27. Garali M, Kahlaoui M, Mohammed B, Mater A, Azouz Cb, Chefi C. Synthesis, characterization and electrochemical properties of $\text{La}_2\text{-xEu}_x\text{NiO}_{4+\delta}$ Ruddlesden-Popper-type layered nickelates as cathode materials for SOFC applications. *International Journal of Hydrogen Energy*. 2019;44(21):11020-32.
28. Usenka A, Pankov V, Vibhu V, Flura A, Grenier J-C, Bassat J-M. Temperature Programmed Oxygen Desorption and Sorption Processes on $\text{Pr}_2\text{-XLaxNiO}_{4+\delta}$ Nickelates. *ECS Transactions*. 2019;91(1):1341-53.
29. Wang C, Soga H, Yugi T, SAKAI M, Okiba T, Hashimoto T. Variation in crystal structure of $\text{Ln}_2\text{Ni}_{1-x}\text{Cu}_x\text{O}_{4+\delta}$ (Ln: La, Pr, Nd, Sm, Eu, and their solid solution) based on type of Ln: Relationship between crystal structure and tolerance factor. *Journal of the Ceramic Society of Japan*. 2019 Oct 1;127(10):678-87.
30. Antonova EP, Stroeveva AY, Tropin ES. Electrode performance of $\text{La}_2\text{NiO}_{4+\delta}$ cathodes in contact with $\text{La}_{0.9}\text{Sr}_{0.1}\text{ScO}_{3-\delta}$ proton-conducting oxide. *Journal of Solid State Electrochemistry*. 2020;24(7):1447-51.
31. Galal A, Atta NF, Hefnawy MA. Lanthanum nickel oxide nano-perovskite decorated carbon nanotubes/poly(aniline) composite for effective electrochemical oxidation of urea. *Journal of Electroanalytical Chemistry*. 2020;862:114009.
32. Antonova EP, Khodimchuk AV, Usov GR, Tropin ES, Farlenkov AS, Khrustov AV, et al. EIS analysis of electrode kinetics for $\text{La}_2\text{NiO}_{4+\delta}$ cathode in contact with $\text{Ce}_{0.8}\text{Sm}_{0.2}\text{O}_{1.9}$ electrolyte: from DRT analysis to physical model of the electrochemical process. *Journal of Solid State Electrochemistry*. 2019;23(4):1279-87.
33. Shen S, Williamson M, Cao G, Zhou J, Tsoi M. Resistive switching in tunnel junctions with a single-crystal La_2NiO_4 electrode. *Journal of Physics D: Applied Physics*. 2019;53(7):075302.
34. Wei M, Che W, Li H, Wang Z, Yan F, Liu Y, et al. Ruddlesden-Popper type $\text{La}_2\text{NiO}_{4+\delta}$ oxide coated by Ag nanoparticles as an outstanding anion intercalation cathode for hybrid supercapacitors. *Applied Surface Science*. 2019;484:551-9.
35. Hinterding R, Zhao Z, Zhang C, Feldhoff A. Anisotropic growth of La_2NiO_4 : Influential pre-treatment in molten-flux synthesis. *Journal of Crystal Growth*. 2019;523:125135.
36. Bouyer F, Sanson N, Destarac M, Gérardin C. Hydrophilic block copolymer-directed growth of lanthanum hydroxide nanoparticles. *New Journal of Chemistry*. 2006;30(3):399.
37. Praveena K, Sadhana K, Srinath S, Murthy SR. Effect of pH on structural and magnetic properties of nanocrystalline $\text{Y}_3\text{Fe}_5\text{O}_{12}$ by aqueous co-precipitation method. *Materials Research Innovations*. 2013;18(1):69-75.
38. Briois P, Perry F, Billard A. Structural and electrical characterisation of lanthanum nickelate reactively sputter-deposited thin films. *Thin Solid Films*. 2008;516(10):3282-6.
39. Fontaine M-L, Laberty-Robert C, Barnabé A, Ansart F, Tailhades P. Synthesis of $\text{La}_2\text{-xNiO}_{4+\delta}$ oxides by polymeric route: non-stoichiometry control. *Ceramics International*. 2004;30(8):2087-98.
40. Wu J, Pramana SS, Skinner SJ, Kilner JA, Horsfield AP. Why Ni is absent from the surface of $\text{La}_2\text{NiO}_{4+\delta}$? *Journal of Materials Chemistry A*. 2015;3(47):23760-7.
41. Egger A, Schrödl N, Gspan C, Sitte W. $\text{La}_2\text{NiO}_{4+\delta}$ as electrode material for solid oxide fuel cells and electrolyzer cells. *Solid State Ionics*. 2017;299:18-25.
42. Jeong C, Lee J-H, Park M, Hong J, Kim H, Son J-W, et al. Design and processing parameters of $\text{La}_2\text{NiO}_{4+\delta}$ -based cathode for anode-supported planar solid oxide fuel cells (SOFCs). *Journal of Power Sources*. 2015;297:370-8.
43. Ferkhi M, Yahia HA. Electrochemical and morphological characterizations of $\text{La}_{2x}\text{NiO}_{4\pm\delta}$ ($x = 0.01, 0.02, 0.03$ and 0.05) as new cathodes materials for IT-SOFC. *Materials Research Bulletin*. 2016;83:268-74.